atoms

MDPI

Article

Visible Light Spectroscopy of W^{14+} Ions in an Electron Beam Ion Trap

Ben Niu [1], Zhaoying Chen [1], Jihui Chen [2], Yanting Li [1], Fangshi Jia [1], Bingli Li [1], Zhencen He [3,4,*], Jun Xiao [1], Yaming Zou [1] and Ke Yao [1]

[1] Shanghai EBIT Laboratory, and Key Laboratory of Nuclear Physics and Ion-Beam Application (MOE), Institute of Modern Physics, Fudan University, Shanghai 200433, China; 19110200019@fudan.edu.cn (B.N.); 23210200001@m.fudan.edu.cn (Z.C.); yantingli18@fudan.edu.cn (Y.L.); 22210200005@m.fudan.edu.cn (F.J.); blli21@m.fudan.edu.cn (B.L.); xiao_jun@fudan.edu.cn (J.X.); zouym@fudan.edu.cn (Y.Z.); keyao@fudan.edu.cn (K.Y.)

[2] Institute of Plasma Physics, Hefei Institutes of Physical Science, Chinese Academy of Sciences, Hefei 230031, China; 20110200021@fudan.edu.cn

[3] West China School of Basic Medical Sciences and Forensic Medicine, Sichuan University, Chengdu 610041, China

[4] Key Laboratory of Radiation Physics and Technology of Ministry of Education, Institute of Nuclear Science and Technology, Sichuan University, Chengdu 610064, China

* Correspondence: hezhencen@scu.edu.cn

Abstract: In this work, the visible lines of W^{14+} ions in the wavelength range of 400–650 nm are investigated experimentally and theoretically. The experiments were performed in a low-energy electron beam ion trap. The simulated spectra of W^{14+} ions (Nd-like) were obtained from atomic structure computations in combination with a collisional–radiative model. Overall, there is a reasonable similarity between the measurements and the results of the simulations, and most of the twelve observed spectral lines associated with W^{14+} were tentatively identified.

Keywords: visible lines; EBIT; tungsten ions

check for updates

Academic Editors: John Sheil and Ronnie Hoekstra

Received: 30 December 2024
Revised: 21 January 2025
Accepted: 3 February 2025
Published: 8 February 2025

Citation: Niu, B.; Chen, Z.; Chen, J.; Li, Y.; Jia, F.; Li, B.; He, Z.; Xiao, J.; Zou, Y.; Yao, K. Visible Light Spectroscopy of W^{14+} Ions in an Electron Beam Ion Trap. *Atoms* **2025**, *13*, 17. https://doi.org/10.3390/atoms13020017

Copyright: © 2025 by the authors. Licensee MDPI, Basel, Switzerland. This article is an open access article distributed under the terms and conditions of the Creative Commons Attribution (CC BY) license (https://creativecommons.org/licenses/by/4.0/).

1. Introduction

The atomic properties of tungsten (W) ions are of strong interest for the diagnostics of magnetic confinement fusion (MCF) plasma, primarily because metallic tungsten is regarded as a promising candidate for armor material in plasma-facing components within MCF devices [1–7] and has been utilized on the diverters of the International Thermonuclear Experimental Reactor (ITER) [1–4], the Experimental Advanced Superconducting Tokamak (EAST) [6,7], and other devices [8,9]. In an MCF device, the interaction between the edge plasma and the plasma-facing components inevitably leads to the widespread existence of W ion impurities throughout the fusion plasma. On one hand, significant radiation power loss from W ion impurities affects the stable operation of MCF plasma [10]. On the other hand, the emission spectra from the W ion impurities are considered one of the essential diagnostic tools for plasma parameters, such as the temperature and density of MCF plasma [11–14]. Consequently, the study of atomic data for W ions such as cross sections and spectral line wavelengths is critically required and holds substantial significance for the diagnosis of MCF plasma. Notably, the forbidden transition lines from highly charged W ions have been applied in the diagnostic study of large helical device (LHD) plasma, attracting extensive attention [13–15].

The visible lines of W^{14+} ions have been investigated both experimentally and theoretically in previous works [16–18]. In 2012, Komatsu et al. [16] measured the visible spectra

of the W^{11+}–W^{28+} ions, and the line at 462.59 nm was identified as a magnetic dipole (M1) transition from W^{14+} ions. In 2015, Kobayashi et al. [17] investigated the visible spectra of W^{12+}–W^{14+} ions, and eleven visible lines with the wavelength range of 340–600 nm were assigned to W^{14+} ions by using the time-of-flight method. Windberger et al. [18] investigated the optical spectra of Nd-like W ions in the wavelength range of 200–800 nm. Their results show a total of twenty optical lines originating from W^{14+} ions. Additionally, Windberger et al. [18] identified nine of these observed lines based on the results of Fock space coupled cluster (FSCC) calculations. However, there are still a lot of unidentified observed lines, which urgently need to be studied.

In the present work, the optical spectra of W^{14+} ions within the wavelength range of 400–650 nm were measured in a low-energy electron beam ion trap (EBIT). The precise charge states of the ions, assigned to the observed line intensities, were analyzed by using a Wien filter device. The theoretical intensities of the spectral lines for W^{14+} ions were simulated with the collisional–radiative model (CRM) method. Based on the comparison between the experimental and theoretical simulated spectra, the identification of the observed optical lines of W^{14+} ions was carried out.

2. Experiment

The current experiments were performed in a low-energy electron beam ion trap CUbic-eBIT(CUBIT) [19–22]. The main components of the CUBIT include an electron gun, an assembly of drift tubes, an electron collector, and a permanent magnet. Inside the CUBIT, the electron beam is emitted from a LaB_6 cathode and accelerated to the required energy by the electrostatic potential difference between the cathode and the central drift tube. Gas-phase atoms and molecules are injected into the drift tube and then ionized to the desired charge states via the electron impact ionization process. The generated highly charged ions are axially confined in a special static potential well formed by the drift tubes, radially trapped by the combination effect of the negative space-charge potential from the electron beam and the axial magnetic field. The ions can be extracted from the trapping region, and the charge state distribution (CSD) can be analyzed with the help of a Wien filter mounted behind the collector. The Wien filter measurement elucidates the charge state of an ensemble of ions by quantifying the time of flight required for the ions to traverse from the trapping region to the detector.

In the present measurements, volatile $W(CO)_6$ was injected into CUBIT through a gas injection system. The emitted light from W ions in the drift tube was projected through a quartz lens with a 100 mm focal length onto the entrance slit of an Andor Shamrock SR-303i Czerny-Turner spectrometer. The photons were dispersed in the spectrometer with 1200 l/mm grating blazed at 300 nm. A charge-coupled device recorded the dispersed light. Each spectrum exposure time was two hours. Each measurement was performed at least five times to minimize random errors. The wavelengths of the spectral lines were calibrated by using gas discharge lamps positioned externally to the CUBIT on the opposite side of the slit.

3. Calculation

The theoretical intensities of the W^{14+} lines were simulated with CRM by using the flexible atomic code (FAC) [23] to identify the observed lines measured in the present work. A concise outline is provided here.

In the current CRM simulation, the FAC was used to obtain all necessary atomic data for constructing the model, such as transition rates, collisional excitation and de-excitation cross sections, level energies, etc. The ground configuration $4d^{10}4f^{12}5s^2$ and a few excited configurations listed in Table 1 were taken into account. A total of 94,260 energy levels

were calculated. Figure 1 shows the lowest 500 energy levels. The lowest 10,000 levels and millions of decay channels (E1, E2, M1, and M2) were taken into account in the CRM calculation. The simulations were conducted with the experiment parameters, i.e., an incident electron beam energy of 300 eV, an electron density of 4×10^{10} cm^{-3}, and three different electron densities of 1×10^{10} cm^{-3}, 4×10^{10} cm^{-3}, and 10×10^{10} cm^{-3}.

Table 1. The configurations considered in our RCI-CRM calculations for W^{14+}.

Ground Configuration	$\mathbf{4d^{10}4f^{12}5s^2}$
Single excitation	$4d^{10}4f^{12}5s5l(l = p,d,f,g)$
	$4d^{10}4f^{12}5s6l(l = s,p,d,f,g)$
	$4d^{10}4f^{11}5s^25l(l = p,d,f,g)$
	$4d^{10}4f^{11}5s^26l(l = s,p,d,f,g)$
	$4d^{9}4f^{12}5s^2nl(n = 5,6; l = p,d,f,g)$
Double excitations	$4d^{10}4f^{13}nl(n = 5,6,7; l = s,p,d,f,g)$
	$4d^{10}4f^{12}5l^2(l = p,d,f,g)$
	$4d^{10}4f^{11}5s5l^2(l = p,d)$
	$4d^{9}4f^{13}5s^2$
	$4d^{9}4f^{13}5s5l(l = p,d,f)$
	$4d^{9}4f^{12}5s5l(l = p,d)$
	$4d^{10}4f^{14}$
	$4d^{10}4f^{10}5s^25l^2(l = p,d)$
	$4d^{10}4f^{10}5s^25p6l(l = s,p,d,f)$
Triple excitations	$4d^{10}4f^{11}5p^3$
	$4d^{9}4f^{13}5p^2$
	$4d^{9}4f^{14}5l(l = s,p,d,f)$
	$4d^{9}4f^{13}5p5l(l = d,f)$
	$4d^{10}4f^{10}5s5p^3$

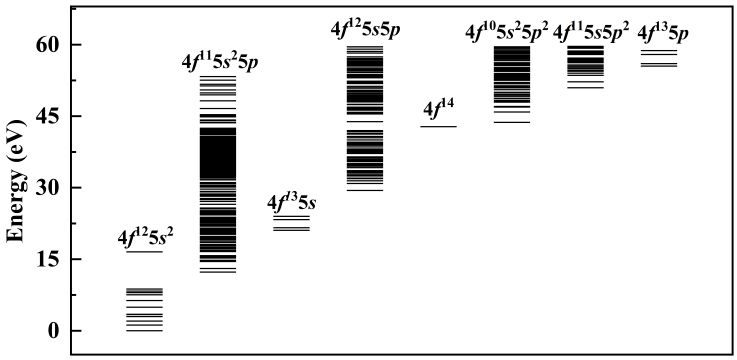

Figure 1. The lowest 500 energy levels of W^{14+} ions calculated by using the RCI method.

4. Results and Discussion

The intensities of the measured spectral lines and CSDs of highly charged W ions at different electron beam energies are shown in Figure 2. The typical optical spectra in the range of 400–650 nm are shown in Figure 2a. No spectral lines of W14+ ions were observed in other parts of the visible light wavelength range in the present work. The lines marked with black arrows in Figure 2a (the labels correspond to Table 2 and Figure 3) respond sensitively to the electron beam energies. Their intensities are linearly dependent on the abundance of W^{14+} ions. Thus, the marked lines indeed belong to W^{14+} ions. Additionally, the lines of W^{14+} ions appeared at 280 eV, which is lower than the ionization threshold of W^{13+} ions (291 eV). It might be the result of ionization from metastable states and has been found in a variety of spectroscopic studies [24,25].

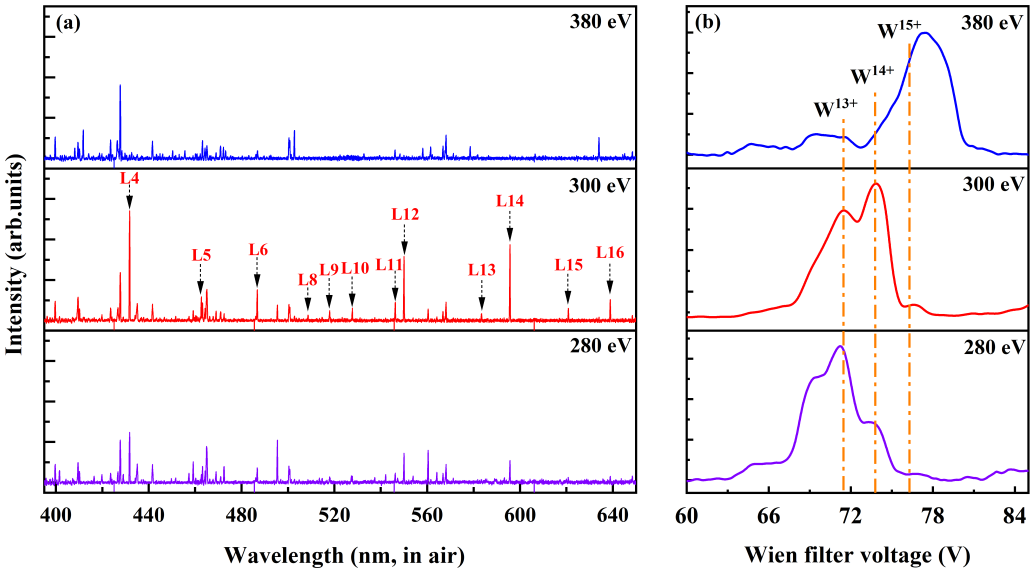

Figure 2. (**a**) The experimental spectra at different electron energies from 280 to 380 eV. The spectra lines indicated by the black arrows are from W^{14+} ions. (**b**) CSDs of W ions at the corresponding electron beam energies.

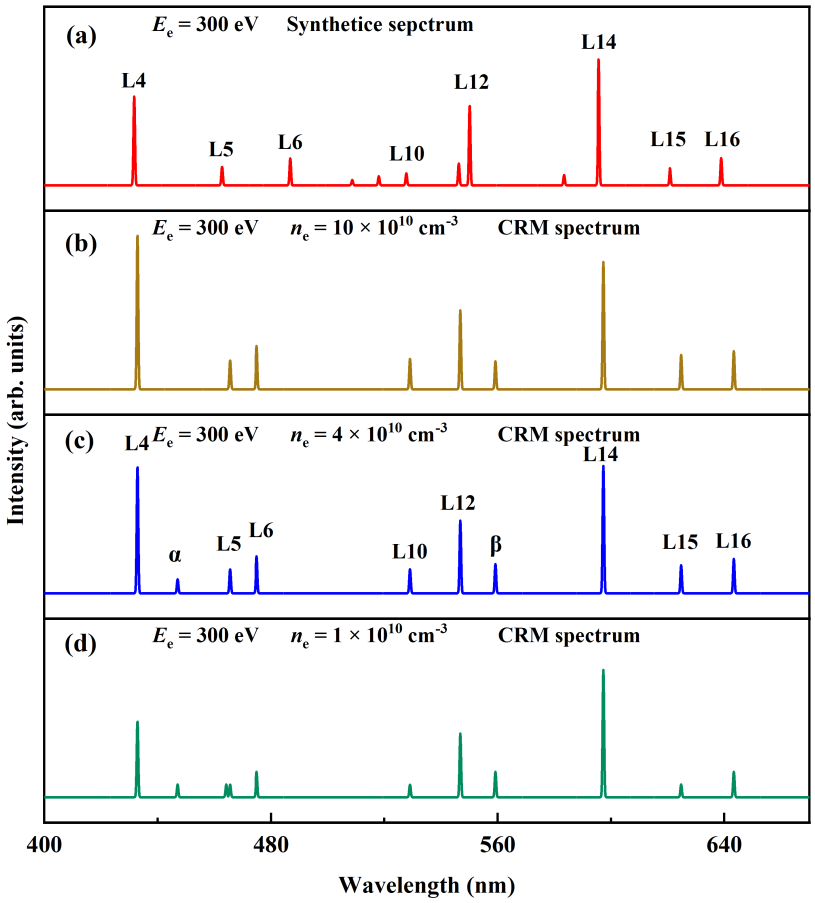

Figure 3. (**a**) The synthetic experimental spectrum of W^{14+} ions at an incident electron energy of 300 eV. (**b**–**d**) Simulated spectra of W^{14+} ions with CRM.

Table 2. Experimental and theoretical wavelengths (nm) by Li et al. [26] and identified transition of Pm-like W^{14+} ions in the optical region. The results reported by Kobayashi et al. [17] and Windberger et al. [18] are also listed for comparison. The columns marked with "*" indicate data measured in this study.

No.	λ^{air} [17]	λ^{air} [18]	I [18]	$\lambda^{air,*}_{expt.}$	$\lambda^{vac,*}_{expt.}$	λ^{vac}_{MCDHF} [26]	Transition
L1		392.36	0.023				
L2		396.12	0.036				
L3		409.43	0.047				
L4	431.75	431.68	0.659	431.74(3)	431.86(3)	432.25	$4f^{12}5s^2\ ^3H_4 \rightarrow\ ^3H_5$
L5	462.59	462.52	0.178	462.56(2)	462.69(2)	465.55	$4f^{12}5s^2\ ^1D_2 \rightarrow\ ^3F_2$
L6	486.57	486.55	0.312	486.59(3)	486.72(3)	474.91	$4f^{12}5s^2\ ^1D_2 \rightarrow\ ^3F_3$
L7	506.40	506.27	0.040				
L8	508.39	508.27	0.061	508.34(3)	508.49(3)		
L9	517.74	517.64	0.100	517.78(2)	517.92(2)		
L10	527.70	527.59	0.136	527.61(2)	527.76(2)	529.00	$4f^{12}5s^2\ ^3P_2 \rightarrow\ ^1D_2$
L11	546.22	546.12	0.178	546.12(2)	546.27(2)		
L12	549.93	549.86	0.710	549.94(2)	550.09(2)	546.81	$4f^{12}5s^2\ ^3F_3 \rightarrow\ ^3F_4$
L13	583.23	583.22	0.107	583.22(3)	583.38(3)		
L14	595.70	595.71	1.000	595.69(2)	595.86(2)	597.30	$4f^{12}5s^2\ ^3H_5 \rightarrow\ ^3H_6$
L15		620.61	0.164	620.60(2)	620.77(2)	624.72	$4f^{12}5s^2\ ^3H_4 \rightarrow\ ^1G_4$
L16		638.63	0.283	638.65(2)	638.83(2)	643.32	$4f^{12}5s^2\ ^1G_4 \rightarrow\ ^3F_4$
L17		686.64	0.047				
L18		691.76	0.011				
L19		717.97	0.004				
L20		735.96	0.004				$4f^{12}5s^2\ ^3H_4 \rightarrow\ ^3F_3{}^*$

Table 2 lists the calibrated spectral line wavelengths in air and vacuum of W^{14+} ions obtained in the present experiments. The reference spectral lines of Ar and Ne ions are shown in Table 3. The numbers in parentheses indicate the experimental wavelength uncertainties, which are given as the sum of the statistical uncertainty and the systematic uncertainties caused by the dispersion function and the external calibration. In addition, the results reported by Kobayashi et al. [17] and Windberger et al. [18] are listed in Table 2. Our results are in good agreement with the reported values. However, several lines reported by Kobayashi et al. [17], including L1–L3, L7, L18, and L19, were not observed in our measurements. This absence is likely due to their relatively low intensities, as indicated by the normalized intensities in the report by Kobayashi et al. [17]. Additionally, lines L19 and L20 fall outside the range of our measurements.

Table 3. The reference spectral lines of Ar and Ne ions which were used to calibrate the W^{14+} spectral lines. All the data represent the Ritz wavelengths (in air) in the NIST database [27].

Ar II	Ar II	Ar II	Ar II	Ar II	Ar II
427.752786(6)	460.956692(7)	465.79009(7)	496.507942(8)	501.716264(8)	514.178260(8)
Ne I	Ne I	Ne I	Ne I	Ne I	Ne I
534.10932(4)	540.05618(4)	585.24879(5)	594.48342(5)	614.30626(5)	633.44278(6)

Figure 3 displays the experimental and simulated spectra of W^{14+} ions at the electron energy of 300 eV. The line intensities were normalized based on line L14. The experimental spectrum of W^{14+} ions shown in Figure 3a is synthesized from different spectral bands. Various corrections, such as the efficiency of the observation window, lens, grating, and CCD detector, were taken into account in the synthesizing procedure. Figure 3b shows the simulated spectra of W^{14+} ions obtained with the CRM at the electron densities of

1×10^{10} cm^{-3}, 4×10^{10} cm^{-3}, and 10×10^{10} cm^{-3}. The typical electron densities were estimated from the equivalent electron density, expressed as [28,29]

$$n_{eff} = \frac{4ln(2)I_e}{\pi e v_e(\tau_e^2 + \tau_i^2)}, \quad (1)$$

where I_e is the electron beam current, e is the charge of an electron, v_e is the speed of electrons, and τ_e and τ_i stand for the diameter of the electron beam and ion cloud, respectively. And τ_e and τ_i were estimated by the broadening of spectral lines. The typical value of the electron density was determined to be in the order of 10^{10} cm^{-3}. The labeled lines with serial numbers in Figure 3b are from the ground configuration $4f^{12}5s^2$. The others, marked α and β, are from the first excited configuration $4f^{11}5s^25p$. To ensure the reliability of line identification based on CRM spectra, the energy levels of the $4f^{12}5s^2$, $4f^{13}5s$, and $4f^{14}$ configurations in the CRM simulation were substituted with the results of the large-scale calculation using the MCDHF and RCI methods by Li et al. [26,30]. It can be seen that the theoretically simulated spectra agree well with the experimental spectrum generally. The eight lines with serial numbers were tentatively identified. Except for line L6, the discrepancies between the calculated and measured wavelengths are within 1%. The details of these identifications are presented in Table 2. Those unidentified observed lines are probably from the $4f^{11}5s^25p$ configuration, which is hard to identify by using the imprecision wavelengths obtained by the RCI calculation. More precise theoretical study in W^{14+} ions is expected in the future. Additionally, it can be seen from Figure 3b that the relative intensity between lines L4 and L14 is sensitive to electron density, which can be a potential candidate to diagnose the electron density of plasma.

Figure 4 presents the energy-level diagram of the lowest 18 levels of W^{14+} ions based on the MCDHF and RCI methods by Li et al. [26,30]. In order to compare our experimental values with theoretical ones, the air wavelength of the W^{14+} line from the experiment was converted into a vacuum value based on the equation proposed by Peck and Reader [31]. It can be seen that except for line L4 from the first excited configuration $4f^{13}5s$ of W^{14+} ions, all the other lines are M1 transitions from the ground configuration $4f^{12}5s^2$ of W^{14+} ions. In addition to direct wavelength comparison, we identifies the lines by using the Ritz combination. Combined with Windberger et al.'s [18] and our identification results, we could conclude that the sum of energies of lines L12 and L20 (the wavelength of line L20 taken by Windberger et al. [18]) is comparable to the sum of energies of lines L15 and L16 within the bounds of experimental uncertainty. Lines L12, L15, and L16 have been identified by the results of CRM calculation in Table 2. Therefore, line L20 can be tentatively identified as the $4f^{12}5s^2\ ^3H_4 \rightarrow\ ^3F_3$ transition of W^{14+} ions.

In the previous study by Windberger et al. [18], line L4 was assigned to blended spectral lines from the $4f^{12}5s^2\ ^3H_4 \rightarrow\ ^3H_5$ transition and $4f^{13}5s\ ^1F_3 \rightarrow\ ^3F_4$ transition of W^{14+} ions. In the present work, it is identified as the $4f^{13}5s^2\ ^3H_4 \rightarrow\ ^3H_5$ transition. The transitions of lines L10 and L20 were attempted to be identified, and the identification results of other lines are in perfect agreement with the results reported by Windberger et al. [18].

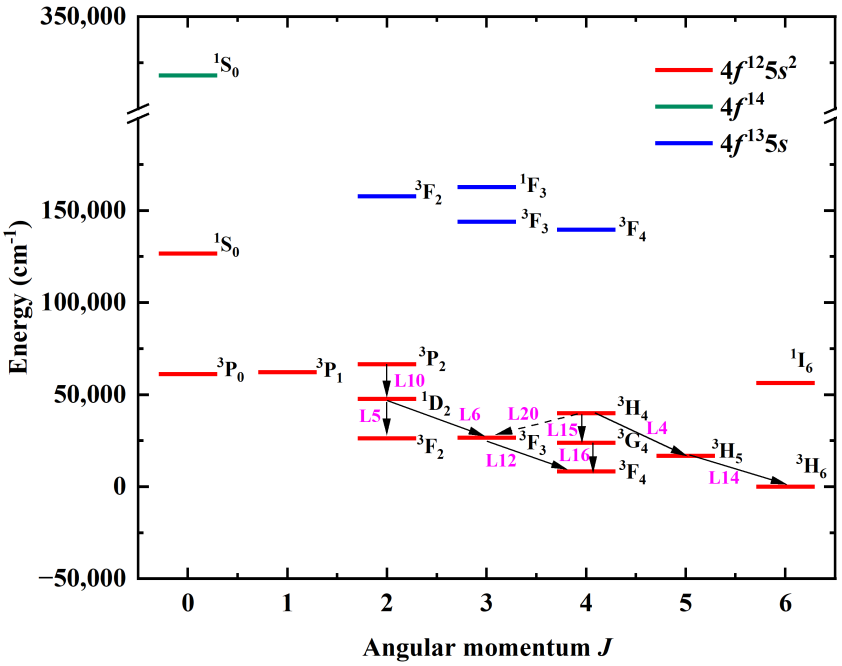

Figure 4. Grotrian diagram for the lowest 18 levels of W^{14+} ions. The black arrows represent the identified M1 transitions observed in the present experiment. The dashed line indicates the line from [18].

5. Conclusions

In summary, a total of twelve optical lines of W^{14+} ions in the wavelength region of 400−650 nm were measured in a low−energy electron beam ion trap. The CRM was employed to simulate the optical spectra of W^{14+} ions, which are in reasonable agreement with the experimental spectra. The corresponding M1 transitions of the nine observed lines were identified. Additionally, some M1 transition lines of W^{14+} ions were found to exhibit dependence on electron density, which can be used for future electron density diagnostics in plasmas.

Author Contributions: Formal analysis, B.N.; Investigation, B.N., Z.C., J.C., Y.L., F.J. and B.L.; Methodology, B.N. and K.Y.; Project administration, Z.H. and K.Y.; Resources, K.Y.; Supervision, Z.H., J.X., Y.Z. and K.Y.; Validation, Z.H. and K.Y.; Writing—original draft, B.N.; Writing—review and editing, Z.C., J.C., Y.L., F.J., B.L., Z.H. and K.Y. All authors have read and agreed to the published version of the manuscript.

Funding: This work was supported by National Key Research and Development Program of China under grant No. 2022YFA1602504 and National Natural Science Foundation of China under grant No. 12304275.

Data Availability Statement: Data are contained within the article.

Conflicts of Interest: The authors declare no conflict of interest.

References

1. Hirai, T.; Carpentier-Chouchana, S.; Escourbiac, F.; Panayotis, S.; Durocher, A.; Ferrand, L.; Garcia-Martinez, M.; Gunn, J.; Komarov, V.; Merola, M.; et al. Design optimization of the ITER tungsten divertor vertical targets. *Fusion Eng. Des.* **2018**, *127*, 66–72. [CrossRef]
2. Litaudon, X.; Abduallev, S.; Abhangi, M.; Abreu, P.; Afzal, M.; Aggarwal, K.M.; Ahlgren, T.; Ahn, J.H.; Aho-Mantila, L.; Aiba, N.; et al. Overview of the JET results in support to ITER. *Nucl. Fusion* **2017**, *57*, 102001. [CrossRef]
3. Pitts, R.; Bonnin, X.; Escourbiac, F.; Frerichs, H.; Gunn, J.; Hirai, T.; Kukushkin, A.; Kaveeva, E.; Miller, M.; Moulton, D.; et al. Physics basis for the first ITER tungsten divertor. *Nucl. Mater. Energy* **2019**, *20*, 100696. [CrossRef]

4. Hirai, T.; Panayotis, S.; Barabash, V.; Amzallag, C.; Escourbiac, F.; Durocher, A.; Merola, M.; Linke, J.; Loewenhoff, T.; Pintsuk, G.; et al. Use of tungsten material for the ITER divertor. *Nucl. Mater. Energy* **2016**, *9*, 616–622. [CrossRef]
5. Neu, R.; Dux, R.; Kallenbach, A.; Pütterich, T.; Balden, M.; Fuchs, J.; Herrmann, A.; Maggi, C.; O'Mullane, M.; Pugno, R.; et al. Tungsten: An option for divertor and main chamber plasma facing components in future fusion devices. *Nucl. Fusion* **2005**, *45*, 209. [CrossRef]
6. Xu, G.; Wang, L.; Yao, D.; Jia, G.; Sang, C.; Liu, X.; Chen, Y.; Si, H.; Yang, Z.; Guo, H.; et al. Physics design of new lower tungsten divertor for long-pulse high-power operations in EAST. *Nucl. Fusion* **2021**, *61*, 126070. [CrossRef]
7. Meng, L.; Xu, J.; Liu, J.; Cao, L.; Wang, P.; Li, A.; Yu, L.; Xu, G.; Wang, L. Development of Langmuir probe array for the new lower tungsten divertor in EAST. *Fusion Eng. Des.* **2022**, *175*, 113011. [CrossRef]
8. Kallenbach, A., for the ASDEX Upgrade Team; the EUROfusion MST1 Team. Overview of ASDEX Upgrade results. *Nucl. Fusion* **2017**, *57*, 102015. [CrossRef]
9. Catarino, N.; Widdowson, A.; Baron-Wiechec, A.; Coad, J.P.; Heinola, K.; Rubel, M.; Barradas, N.P.; Alves, E.; Contributors, J. Deposition in the tungsten divertor during the 2011–2016 campaigns in JET with ITER-like wall. *Phys. Scr.* **2020**, *2020*, 014044. [CrossRef]
10. Philipps, V. Plasma-wall interaction, a key issue on the way to a steady state burning fusion device. *Phys. Scr.* **2006**, *T123*, 24–32. [CrossRef]
11. Beiersdorfer, P.; Clementson, J.; Safronova, U.I. Tungsten data for current and future uses in fusion and plasma science. *Atoms* **2015**, *3*, 260–272. [CrossRef]
12. Rzadkiewicz, J.; Yang, Y.; Kozioł, K.; O'Mullane, M.G.; Patel, A.; Xiao, J.; Yao, K.; Shen, Y.; Lu, D.; Hutton, R.; et al. High-resolution tungsten spectroscopy relevant to the diagnostic of high-temperature tokamak plasmas. *Phys. Rev. A* **2018**, *97*, 052501. [CrossRef]
13. Kato, D.; Sakaue, H.A.; Murakami, I.; Goto, M.; Oishi, T.; Tamura, N.; Funaba, H.; Morita, S. Assessment of W density in LHD core plasmas using visible forbidden lines of highly charged W ions. *Nucl. Fusion* **2021**, *61*, 116008. [CrossRef]
14. Fujii, K.; Takahashi, Y.; Nakai, Y.; Kato, D.; Goto, M.; Morita, S.; Hasuo, M.; Group, L.E. Visible emission spectroscopy of highly charged tungsten ions in LHD: II. Evaluation of tungsten ion temperature. *Phys. Scr.* **2015**, *90*, 125403. [CrossRef]
15. Shinohara, M.; Fujii, K.; Kato, D.; Nakamura, N.; Goto, M.; Morita, S.; Hasuo, M.; Group, L.E. Visible emission spectroscopy of highly charged tungsten ions in LHD: I. Survey of new visible emission lines. *Phys. Scr.* **2015**, *90*, 125402. [CrossRef]
16. Komatsu, A.; Sakoda, J.; Minoshima, M.; Sakaue, H.; Ding, X.; Kato, D.; Murakami, I.; Koike, F.; Nakamura, N. Visible Transitions in Highly Charged Tungsten Ions: 365–475 nm. *Plasma Fusion Res.* **2012**, *7*, 1201158. [CrossRef]
17. Kobayashi, Y.; Kubota, K.; Omote, K.; Komatsu, A.; Sakoda, J.; Minoshima, M.; Kato, D.; Li, J.; Sakaue, H.A.; Murakami, I.; et al. Extreme ultraviolet and visible spectroscopy of promethiumlike heavy ions. *Phys. Rev. A* **2015**, *92*, 022510. [CrossRef]
18. Windberger, A.; Crespo López-Urrutia, J.R.; Bekker, H.; Oreshkina, N.S.; Berengut, J.C.; Bock, V.; Borschevsky, A.; Dzuba, V.A.; Eliav, E.; Harman, Z.; et al. Identification of the Predicted $5s-4f$ Level Crossing Optical Lines with Applications to Metrology and Searches for the Variation of Fundamental Constants. *Phys. Rev. Lett.* **2015**, *114*, 150801. [CrossRef] [PubMed]
19. He, Z.; Meng, J.; Li, Y.; Jia, F.; Khan, N.; Niu, B.; Huang, L.; Hu, Z.; Li, J.; Wang, J.; et al. Magnetic-dipole lines in Fe-like and Mn-like molybdenum ions. *J. Quant. Spectrosc. Radiat. Transf.* **2022**, *288*, 108276. [CrossRef]
20. Li, Y.; Wang, Y.; Fan, J.; Si, R.; Li, J.; Zhang, M.; Huang, L.; Xiao, J.; Zou, Y.; Wei, B.; et al. Precise wavelength determination of the $4s^2 4p\ ^2P_{3/2}$-$^2P_{1/2}$ transition in Mo^{11+} and Ru^{13+} ions. *J. Phys. B At. Mol. Opt. Phys.* **2022**, *54*, 235001. [CrossRef]
21. Wang, Y.; Li, Y.; Liu, J.; Jia, F.; Si, R.; Zhang, M.; Huang, L.; Tu, B.; Zou, Y.; Wei, B.; et al. Direct wavelength measurement of the $4p^2\ ^3P_1 -^3 P_0$ highly charged ion clock transition in Rh^{13+}. *J. Quant. Spectrosc. Radiat. Transf.* **2022**, *293*, 108370. [CrossRef]
22. Niu, B.; Li, Y.; Xiong, G.; Chen, J.; Hu, Z.; Fu, Y.; Zou, Y.; Chen, C.; Yao, K. The magnetic dipole transition in Rb-like ion and its core-valence correlation effect. *J. Quant. Spectrosc. Radiat. Transf.* **2024**, *312*, 108812. [CrossRef]
23. Gu, M.F. Indirect X-Ray Line-Formation Processes in Iron L-Shell Ions. *Astrophys. J.* **2003**, *582*, 1241. [CrossRef]
24. Lu, Q.; He, J.; Tian, H.; Li, M.; Yang, Y.; Yao, K.; Chen, C.; Xiao, J.; Li, J.G.; Tu, B.; et al. Observation of indirect ionization of W^{7+} in an electron-beam ion-trap plasma. *Phys. Rev. A* **2019**, *99*, 042510. [CrossRef]
25. Mita, M.; Sakaue, H.A.; Kato, D.; Murakami, I.; Nakamura, N. Extreme ultraviolet spectra of multiply charged tungsten ions. *J. Phys. Conf. Ser.* **2017**, *875*, 012019. [CrossRef]
26. Li, Y.; et al. Institute of Modern Physics, Fudan University, Shanghai, China, 2025, manuscript in preparation.
27. Kramida, A.; Ralchenko, Y.; Reader, J.; NIST ASD Team. NIST Atomic Spectra Database (Version 5.12). 2024. Available online: https://physics.nist.gov/asd (accessed on 1 January 2024.) .
28. Arthanayaka, T.; Beiersdorfer, P.; Brown, G.; Hahn, M.; Hell, N.; Lockard, T.; Savin, D.W. Measurements of the effective electron density in an electron beam ion trap using extreme ultraviolet spectra and optical imaging. *Rev. Sci. Instrum.* **2018**, *89*, 10E119. [CrossRef] [PubMed]
29. Arthanayaka, T.; Beiersdorfer, P.; Brown, G.V.; Gu, M.F.; Hahn, M.; Hell, N.; Lockard, T.; Savin, D.W. Laboratory calibrations of Fe XII–XIV line-intensity ratios for electron density diagnostics. *Astrophys. J.* **2020**, *890*, 77. [CrossRef]

30. Jönsson, P.; Godefroid, M.; Gaigalas, G.; Ekman, J.; Grumer, J.; Li, W.; Li, J.; Brage, T.; Grant, I.P.; Bieroń, J.; et al. An Introduction to Relativistic Theory as Implemented in GRASP. *Atoms* **2023**, *11*, 7. [CrossRef]
31. Peck, E.R.; Reeder, K. Dispersion of Air*. *J. Opt. Soc. Am.* **1972**, *62*, 958–962. [CrossRef]

Disclaimer/Publisher's Note: The statements, opinions and data contained in all publications are solely those of the individual author(s) and contributor(s) and not of MDPI and/or the editor(s). MDPI and/or the editor(s) disclaim responsibility for any injury to people or property resulting from any ideas, methods, instructions or products referred to in the content.